Eur. J. Mineral., 33, 687–702, 2021
https://doi.org/10.5194/ejm-33-687-2021

European Journal of Mineralogy
Open Access

Characterization and origin of the Mn-rich patinas formed on Lunéville château sandstones

Laure Gatuingt[1,2,3], Stéphanie Rossano[1], Jean-Didier Mertz[2,3], Chloé Fourdrin[1], Olivier Rozenbaum[4], Quentin Lemasson[5], Solenn Reguer[6], Nicolas Trcera[6], and Bruno Lanson[7]

[1]Laboratoire Géomatériaux et Environnement, Univ. Gustave Eiffel, 77454 Marne-La-Vallée, France
[2]Laboratoire de Recherche des Monuments Historiques, 77420 Champs-sur-Marne, France
[3]Centre de Recherche sur la Conservation, USR3224, Sorbonne université, 75005 Paris, France
[4]CEMHTI UPR3079, CNRS, Univ. Orléans, 45071 Orléans, France
[5]Centre de Recherche et de Restauration des Musées de France, Fédération de Recherche NewAGLAE, FR3506 CNRS, Ministère de la Culture, Chimie ParisTech, Palais du Louvre, 75001 Paris, France
[6]Synchrotron SOLEIL, L'Orme des Merisiers Saint-Aubin, BP 48, 91192 Gif-sur-Yvette, France
[7]ISTerre, Univ. Grenoble Alpes, CNRS, Univ. Savoie-Mont Blanc, IRD, Univ. Gustave Eiffel, 38041 Grenoble, France

Correspondence: Laure Gatuingt (laure.gatuingt@gmail.com) and Bruno Lanson (bruno.lanson@univ-grenoble-alpes.fr)

Received: 4 May 2021 – Revised: 26 September 2021 – Accepted: 8 October 2021 – Published: 11 November 2021

Abstract. The formation of iron- and/or manganese-rich dark patinas on sandstones is a common natural phenomenon that occurs also on building stones. Lunéville château, in eastern France, presents such patinas that developed either under natural conditions (rain and time) or after an accidental fire and exposure to significant amounts of water as part of attempts to extinguish the fire. The present study aimed at characterizing both types of patinas in an effort to determine their formation mechanisms and Mn sources. In both cases, Mn required for patina formation likely derives from the reductive dissolution of Mn-rich minerals present in pristine sandstones, as suggested by the contrasting mineralogy and chemistry of Mn-rich phases present in the bulk and in the patina of a given building block. Reduced Mn species then migrate to the exposed surface of building blocks where they are re-oxidized via undetermined processes. Patinas developing "naturally" over time result from the alternation of wetting-reducing and drying-oxidizing cycles and appear to be composed of birnessite. Patinas formed after the 2003 fire result from this single accidental event and form a much thinner, heterogeneous, and discontinuous layer of poorly crystalline lithiophorite at the sandstone surface (∼ 0–150 µm compared to ∼ 300–600 µm for "natural" patinas). The lack of Mn-rich patinas on areas of Lunéville château is likely related to the lower Mn content of pristine sandstone blocks.

1 Introduction

Lunéville château was built during the 18th century in northeastern France with local Buntsandstein sandstones of various colors (yellow, grey, and sometimes red). In January 2003, a violent fire affected the roof of the château, and the building was exposed to substantial amounts of water (∼ 21 m^3 min^{-1} for ∼ 10 h) as part of the attempts to extinguish the fire. Several weeks later, black-brown stains appeared on burnt parts of the château (Fig. 1). In 2014, based on a photographic analysis of the external surfaces of the château's walls, ∼ 8 % of exposed surfaces were estimated to be stained. Due to the attention paid to the building following the appearance of these dark stains, dark brown patinas were also detected in areas of the building that were not affected by the accidental fire, suggesting that these patinas predated the fire. Repeated attempts to remove these dark patinas during the restoration of Lunéville château were unsuccessful, giving a soiled and unsightly aspect to the château.

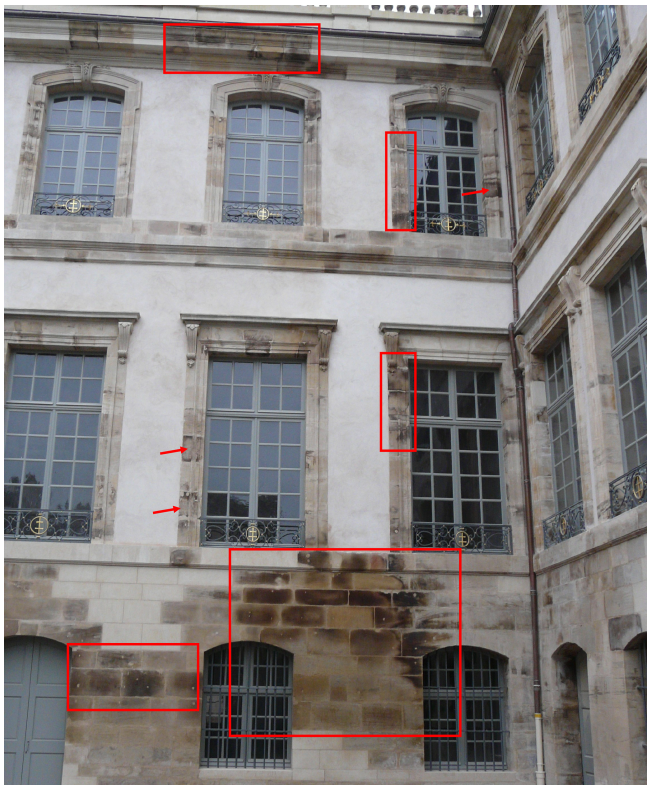

Figure 1. Examples of patinas developed on Lunéville château sandstones after the 2003 fire (red arrows and outlines). The picture is dated from December 2014, after restoration.

Similar-looking thin black layers were previously observed on monuments built from granite or sandstone. These dark layers most often consist of Fe-(oxihydr)oxides (Nord and Ericsson, 1993; Thomachot and Jeannette, 2004; Mertz, 2010) and/or Mn-(oxihydr)oxides (Vicenzi et al., 2016; Sharps et al., 2020), but their precise mineralogical composition and their formation mechanisms often remain elusive. There are only a few studies on the appearance and origin of such dark layers on architectural stones (Nord and Ericsson, 1993; Vicenzi et al., 2016; Sharps et al., 2020). One hypothesis is that Fe and/or Mn comes from the underlying rock, being solubilized by rainwater; subsequently, Fe and/or Mn migrates and precipitates onto the surface rock (Nord and Ericsson, 1993). Alternatively, aeolian deposition has also been proposed as a possible source for Mn and associated elements (e.g., Ba, Pb, Zn) that compose the black layer on the Smithsonian Castle (Washington, DC; Sharps et al., 2020) or on the Freiburger Münster (Freiburg, Germany; Macholdt et al., 2017). Dark layers on sandstone surfaces found in natural environments (rock/desert varnish) are mainly composed of clay minerals and poorly crystallized Fe- and Mn-(oxihydr)oxides (Engel and Sharp, 1958; Potter and Rossman, 1979; Krumbein and Jens, 1981; McKeown and Post, 2001; Dorn, 2007; Garvie et al., 2008). These compounds seem to form from local element sources, such as dust, which can be solubilized by dew or rain. Soluble Fe and/or Mn ions then migrate to the rock surface, where new Fe and/or Mn compounds precipitate (Thiagarajan and Lee, 2004; Dorn, 2007; Garvie et al., 2008; Goldsmith et al., 2014; Macholdt et al., 2015). The formation of these thin black layers is not fully understood, however, although both biotic and abiotic formation models have been proposed in the literature (Krumbein and Jens, 1981; Dorn, 2007).

In the present case, an unpublished preliminary study revealed that dark phases are enriched in manganese but failed to unravel their precise nature, thus impeding the development of an efficient remediation strategy. The present work aims at further characterizing these Mn-rich patinas and the underlying bulk sandstones from both burnt and unburnt parts of the Lunéville château. Chemical information was obtained from particle-induced X-ray emission (PIXE) spectroscopy experiments, whereas optical microscopy (OM) and scanning electron microscopy coupled with energy dispersive X-ray spectroscopy (SEM-EDS) were used to characterize sample (micro-)morphology. In addition, micro-Raman spectroscopy (μ-Raman spectroscopy), micro-X-ray diffraction (μ-XRD), and micro-X-ray absorption near edge structure (μ-XANES) spectroscopy were combined to investigate the nature of the Mn-bearing phases and the oxidation state of Mn in both the bulks and the patinas. Sandstone bulk samples were also studied and compared to unravel patina formation mechanisms since variations in sandstone transfer properties such as porosity and permeability, and in turn ease of rainwater access, do not account for their contrasting behaviors (Gatuingt et al., 2016).

2 Materials and methods

2.1 Samples

Three sandstone blocks (L1, L2, and L4), $\sim 20 \times 30 \times 10\,\mathrm{cm}^3$ in size, extracted from Lunéville château are shown in Fig. 2, whereas their location is reported in Fig. 3. L1 comes from an unburnt area and exhibits patina on its surface (Figs. 2a, 3). According to Lunéville residents, the L1 patina has been present for several decades. The L2 block, which also presents a patina, comes from an area subjected to the 2003 fire and was thus exposed to substantial amounts of water. On this block, mortar has been used to fill some surface areas for reparation and joints (Figs. 2b, 3). In addition, a sandstone block devoid of patina (L4) was extracted from an unburnt area of the château to be used as a control sample (Figs. 2c, 3). In the unburnt parts of the château, blocks exhibiting patina prevail in areas exposed to rain, run-off, and seepage water and/or water capillary rise at the bottom of the building. In these areas, patina is not observed on all blocks, however. Similarly, in the part of the château exposed to the 2003 fire, although

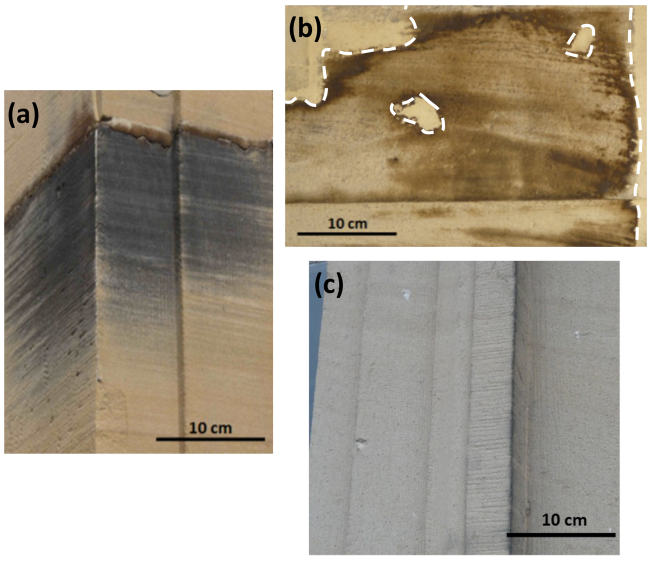

Figure 2. Macroscopic views of the extracted blocks. **(a)** L1: sandstone with patina from an unburnt zone. **(b)** L2: sandstone with patina from a burnt and highly watered zone. Dotted white lines indicate the interface between L2 sandstone and mortar used for reparations and joints. **(c)** L4: patina-free sandstone from an unburnt zone.

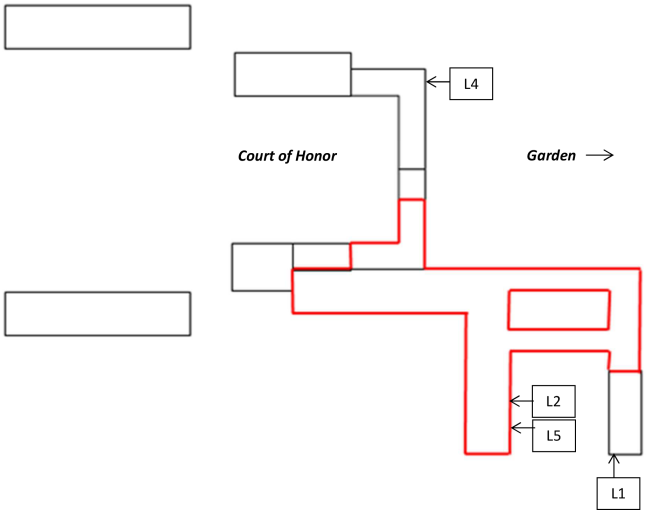

Figure 3. Sketch of the Lunéville château with the original location of blocks L1, L2, L4, and L5 – not presented here (Gatuingt, 2017): L1 was located in the frame of an opening on the ground floor of the edifice, L4 in the frame of a second floor window, and L2 and L5 on the same balustrade on the first floor, a few blocks apart from each other. The zone in red represents the zone affected by the 2003 fire.

more frequent than in unburnt areas, patina is not present on all sandstone blocks, with adjacent blocks being affected or not (Fig. S1 in the Supplement). No specific influence of the orientation was observed on the occurrence of patinas. Hereafter, "surface" stands for the interface between the atmosphere and the building stone. For both L1 and L2, a patina is present on the surface. "Bulk" refers to the inside of the sandstone block, patina excluded, whereas "subsurface" describes the superficial part of the bulk and corresponds to a < 2 cm distance from the surface.

For each block, several samples were prepared to perform the experiments, as schematized in Fig. 4. Two pairs of samples ($\sim 2 \times 2 \times 1\,\mathrm{cm}^3$) were cut perpendicular to the block surface, embedded in resin, and prepared as polished sections (Fig. 4a). For each pair, the first section is representative of the bulk, whereas the second includes the surface and subsurface of the block. One pair of polished sections was studied with OM and SEM-EDS, whereas the other one was used for µ-XANES measurements. The µ-XRD analysis of the Mn-rich zones from the bulks was performed on thin sections ($\sim 2 \times 3\,\mathrm{cm}^2$ and 30 µm thick) prepared from cross sections extracted from the bulks (Fig. 4b). The µ-XRD analysis of the patinas was performed on powders scraped from L1 and L2 patinas and fixed on a Kapton tape (Fig. 4c). One unpolished cross section ($\sim 2 \times 2 \times 1\,\mathrm{cm}^3$) was taken from each block core for PIXE chemical analysis (Fig. 4d). Two additional samples ($\sim 1 \times 0.5 \times 0.5\,\mathrm{cm}^3$) were collected from each block surface (Fig. 4e): one was used for PIXE chemical analyses of the surfaces and the other for mineralogical characterization of Mn phases from the surfaces. Finally, a sandstone slice ($\sim 5 \times 5 \times 1\,\mathrm{cm}^3$) was cut perpendicular to the surface of each block and analyzed with µ-Raman spectroscopy (Fig. 4f). These slices included both the surface and the bulk of the sandstone blocks.

2.2 Particle-induced X-ray emission spectroscopy

PIXE analyses were performed at the AGLAE (Accélérateur Grand Louvre d'Analyse Elémentaire, Paris) facility (Pichon et al., 2014) using a proton energy of 3 MeV and a beam size of 20 µm for the surfaces and of 50 µm for the bulks. The analyzed area was $\sim 1\,\mathrm{mm}^2$ for the surfaces and $\sim 5 \times 5\,\mathrm{mm}^2$ for the bulks, with a beam penetration of ~ 50 µm that allows for limiting the contribution of the bulk to the obtained surface compositions. All compositions were normalized to 100 %, part of the quantified elements being reported hereafter.

2.3 Microscopies

Optical micrographs were obtained with a Keyence VHX-5000 microscope using a $\times 100$ magnification, whereas SEM images were obtained with a JEOL JSM 5600 LV equipped with a tungsten filament using an accelerating voltage of 20 kV and a low vacuum pressure (17 Pa) to avoid sample coating.

Mn-rich areas were selected using visual criteria for µ-Raman, µ-XRD, and µ-XANES measurements. Mn-rich minerals being especially sensitive to beam damage, special attention was paid to avoid interactions between X-ray or laser

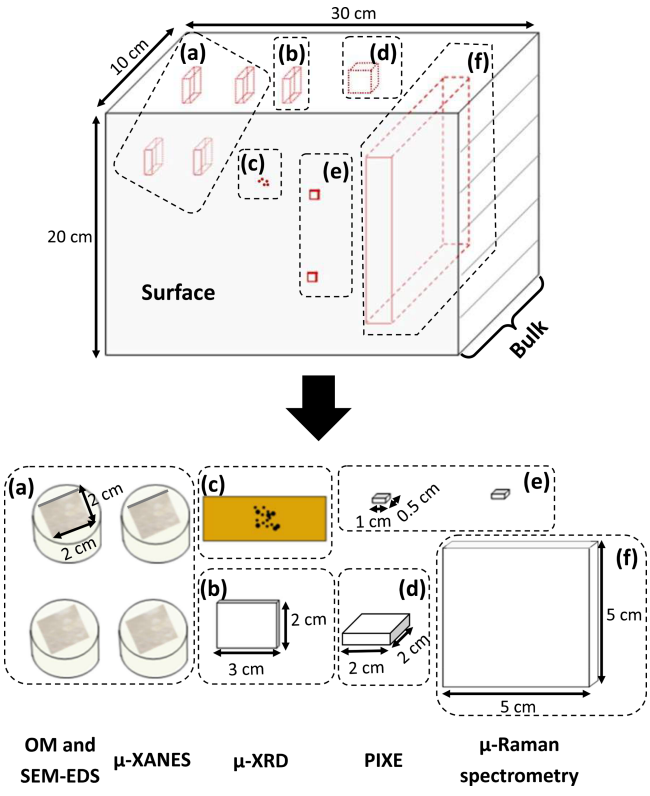

Figure 4. Schematic views of the different samples prepared from a given block for analyses. "Surface" stands for the interface between the atmosphere and the building stone. "Bulk" refers to the inside of the sandstone block, patina excluded. **(a)** $2 \times 2\,cm^2$ samples embedded in resin for optical microscopy, SEM-EDS, and μ-XANES; **(b)** $2 \times 3\,cm^2$ thin strip and **(c)** patina powder for XRD; **(d)** $2 \times 2\,cm^2$ sample for PIXE; **(e)** $1 \times 0.5\,cm^2$ surface samples for PIXE and μ-Raman spectroscopy; **(f)** $5 \times 5\,cm^2$ slice for μ-Raman spectroscopy.

beams and the regions of interest (ROIs) prior to the analyses. When possible, ROIs were selected at different distances from the surface to assess the eventual evolution of Mn oxidation state and/or of Mn mineralogy. Concerning the patinas, different ROIs were selected to average the information. Within a given ROI, several points were measured to assess homogeneity. For μ-XRD and μ-XANES, these points were selected from a quick micro X-ray fluorescence map of the ROI obtained with a low current intensity to maximize contribution from Mn-bearing phases.

2.4 μ-Raman spectroscopy

Raman spectra were collected using a Renishaw inVia confocal microscope equipped with a 532 nm laser. The laser beam was focalized through a long distance ×50 objective, and the theoretical size of the spot on the sample was below $1\,\mu m^2$. The instrument was calibrated by recording the Raman spectrum of silicon. As Mn oxides are very sensitive to the laser beam (Julien et al., 2003, 2004; Baddour-Hadjean and Pereira-Ramos, 2010; Post et al., 2020), special care was taken to avoid artifacts due to degradation effects. Data collection thus began using a very low power (50 μW) and an average of 30 scans of 1 s each (30×1 s). If no evolution of the spectra was detected, the number of scans was steadily increased (up to 2000×1 s), together with the laser power, to improve the signal-to-noise ratio. A total of 200 or 2000 scans (1 s each) recorded with a laser excitation power of 500 or 50 μW, depending on sample stability, were averaged to obtain the final spectra. These spectra were collected from ~ 60 to $1800\,cm^{-1}$ with a $1.56\,cm^{-1}$ step size. Following baseline removal (WIRE 3.4 software), spectra were normalized to the strongest peak in the 500–700 cm^{-1} range, which corresponds to Mn–O stretching modes in MnO_6 octahedra (Julien et al., 2004; Baddour-Hadjean and Pereira-Ramos, 2010).

2.5 μ-X-ray diffraction

The μ-XRD patterns were collected in transmission mode on DiffAbs beamline (SOLEIL synchrotron facility, Saint-Aubin, France) using a 2D XPAD detector and a microfocused beam ($5 \times 9\,\mu m^2$). Beam energy was set to 18 keV (i) to be high enough to ensure that the beam goes across the sample, (ii) to minimize degradation of the Mn-bearing phases, and (iii) to be low enough to minimize data collection time without hindering phase identification due to diffraction peak tightening. Data were collected for 30 s at each of the 26 detector positions used. XRD patterns were collected from 6.32 to 36.58° 2-theta (i.e., between 6.25 and 1.1 Å), with a 0.02° integration step. Data were processed with Bruker EVA software, and phase identification was performed with the PDF-2004 database.

2.6 μ-X-ray absorption near edge structure (XANES) spectroscopy

XANES spectra were collected at the Mn K-edge on the LUCIA beamline (SOLEIL synchrotron facility, Saint-Aubin, France) using the fly-scan mode and fluorescence detection. To minimize photoreduction effects commonly reported for Mn-bearing phases (Bargar et al., 2005; Manceau et al., 2012; Ferrand, 2014; Ferrand et al., 2015), the beam size used was $50 \times 50\,\mu m^2$, and the photon flux was reduced together with data collection time. XANES spectra were collected from 6505 to 6630 eV with a 0.2 eV step size, and 0.4 s counting time per step. Using these conditions, beam intensity was 25 μA (2.2×10^{11} photons s^{-1}). A total of 10 spectra were collected at each point and averaged when similar to each other. At the K-edge, Mn oxidation state can be assessed from the position and shape of pre-edge features, edge position varying significantly from one compound to another for a given oxidation state (Manceau et al., 1992, 2012; Chalmin, 2003; Farges, 2005; Ferrand, 2014; Ferrand et al., 2015). Mn

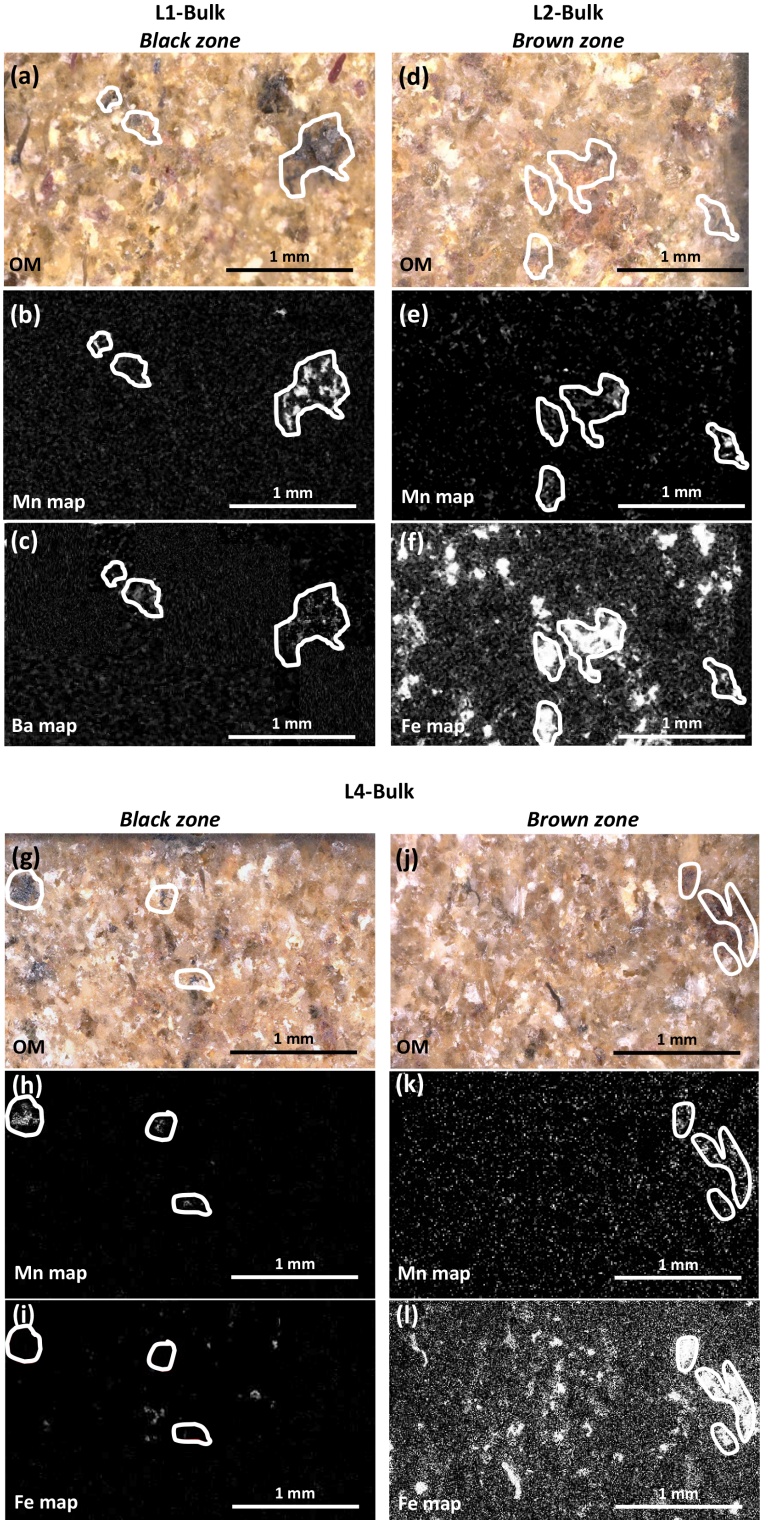

Figure 5. Optical images (**a, d, g, j**) and EDS maps (**b, c, e, f, h, i k, l**) obtained on selected zones from the bulks of L1 (**a, b, c**), L2 (**d, e, f**), and L4 (**g, h, i, j, k, l**). In the chemical maps, bright areas indicate high elemental concentrations (Mn: **b, e, h, k**; Ba: **c**; Fe: **f, i, l**). Mn-rich zones are outlined in white to reveal possible positive correlations with other elements.

oxidation state was also determined using the Combo method (Manceau et al., 2012). To this purpose, experimental spectra were corrected (6505–6630 eV energy range, shift in energy, correction of the deformation due to the fluorescence mode, normalization) prior to fitting their derivative (EXAFS linear least-squares fit software) with the set of 17 reference spectra proposed by Manceau et al. (2012). The resulting average oxidation state was systematically compared to the shape of the pre-edge to ensure its consistency. Uncertainties in the proportions of the different Mn oxidation states (II, III, IV) were determined from the extreme proportions obtained for combinations fitting the data with a residue not exceeding the best fit residue by more than 10 %.

3 Results

3.1 Sample characterization

The three sandstones (Fig. 2) exhibit similar quartz grain size ($\sim 400\,\mu m$) and present a yellowish tint, although L4 color is less pronounced than that of L1 and L2. Except for a few dark spots due to soiling, the surface of L4 is lightly colored and homogeneous (Fig. 2c), whereas L1 and L2 surfaces are heterogeneous with darker zones typical of patina. The L1 patina (Fig. 2a) is black with a metallic sheen, and visual differentiation of areas with or without patina is easy. By contrast, the L2 patina is brown and covers the whole block surface (Fig. 2b), however, with heterogeneous color intensity. Specifically, the L2 patina appears darker at the contact with mortar zones.

Chemical compositions of all samples were obtained from PIXE measurements (Table 1). With $[SiO_2]$ ~ 80 wt %–90 wt %, $[Al_2O_3]$ ~ 5 wt %–10 wt %, $[K_2O]$ ~ 3 wt %–5 wt %, and significative Fe contents ($[Fe_2O_3] > 0.8$ wt %), bulk compositions of the three blocks are consistent with those reported for Buntsandstein sandstones (Beyer, 1983; Kosaka, 1995; Thomachot, 2002; Colas, 2011). Mn is present as a minor element in all blocks ($0.04\,wt\,\% \leq [MnO] \leq 0.10$ wt %; Table 1), although about twice more abundant in L1 and L2 bulks than in L4 bulk. Bulk composition of L1 contrasts also with those of L2 and L4 by its twofold Ba content (Table 1).

Compared to the bulks, surface compositions exhibit lower SiO_2 contents (Table 1), most probably as the result of dilution effects. Irrespective of the presence of patina, surfaces are enriched in S and Ca compared to bulk compositions (Table 1), possibly as the result of sulfate (gypsum) precipitation, frequent on building stones (Schaffer, 1932; Siegesmund et al., 2002; Thomachot, 2002; Gaviño et al., 2005; Marszalek et al., 2014). The surface of L1 does not exhibit such S enrichment, however. This "absence" does not appear to be linked to the long-term development of the patina and is more likely related to an increased sulfur leaching by rain, run-off, and seepage water. P contents are similar in all analyzed surfaces, and differences observed for Al, K, Fe, and Ti from one surface to the other do not exceed the heterogeneity expected for Buntsandstein sandstones (Beyer, 1983; Colas, 2011; Soyk, 2015). These elements (Si, Ca, S, P, Al, K, Fe, Ti) are thus likely not relevant to discriminate L1 and L2 patinas. In particular there is no systematic increase in the Fe content in the patina compared to that of the bulk of the respective block. Similarly, no systematic relation was observed between the initial Fe content of the bulk sandstone and the development of a patina at the block surface, the Fe content of L4 bulk being intermediate between those of L1 and L2 (Table 1). Ba content in the L1 patina is higher than the one found in the bulk (Table 1). Similarly, L1, L2, and L4 surfaces appear enriched in Mg and Na compared to the bulks, the tendency being more pronounced for the two surfaces exhibiting a patina. These elemental enrichments are to be considered carefully as compositional variations could be due to Buntsandstein sandstone heterogeneity. Consistent with preliminary observations (Gatuingt et al., 2016; Gatuingt, 2017), surfaces with a patina are significantly enriched in Mn compared to the bulks, with $\times 47$ and $\times 15$ enrichment factors for L1 and L2, respectively (Table 1), the Mn content in the L1 patina being about fourfold that in the L2 patina.

Mn-rich areas within the sandstone bulks were characterized from OM and SEM-EDS observations on polished sections that systematically show clustering of Mn-rich compounds in specific dark-colored zones (Fig. 5). L1 contains numerous black zones (Fig. 5a–c), with a diameter of $\sim 500\,\mu m$, disseminated through the bulk and enriched in Mn and Ba compared to lighter areas. By contrast, the numerous brown areas present in L2 bulk (Fig. 5d–f) are enriched in Fe and occasionally also in Mn. These brown areas range from hundreds of micrometers to several centimeters in diameter. Although seemingly less frequent than in L1 and L2 bulks, both black and brown zones with diameters of hundreds of micrometers are visible in L4 (Fig. 5g–l). L4 black and brown zones are enriched in Mn, without Ba however, and in Fe and Mn, like L2 brown zones, respectively. Within a given block, Mn-rich areas show no morphological or chemical evolution as a function of the distance from the block surface.

OM micrographs and SEM-EDS elemental maps of polished sections cut perpendicular to surfaces with patina are shown in Fig. 6. The L1 patina appears as a continuous ~ 300–$600\,\mu m$ thick black layer, whereas L2 patina thickness varies from ~ 0 to $150\,\mu m$ and does not cover the whole surface (Fig. 6a and d, respectively), consistent with macroscopic observations (Fig. 2). In both cases, elemental Mn maps show that patinas do not uniformly coat block surfaces, but Mn phases are rather inlaid between subsurface grains. Consistent with global chemical analyses (Table 1), both L1 and L2 patinas are enriched in Mn compared to the subsurface (Fig. 6b, e) but contain no Ba or Fe (Fig. 6c, f), in contrast to the elemental correlations observed in Mn-rich zones of corresponding bulks (Fig. 5c, f).

Table 1. Chemical composition (oxide wt %) of L1, L2, and L4 bulks and surfaces obtained by PIXE.

	L1-Bulk	L1-Patina	L2-Bulk	L2-Patina	L4-Bulk	L4-Surface
SiO_2	84.94 ± 0.27	73.20 ± 0.39	84.47 ± 0.26	70.82 ± 0.36	84.62 ± 0.26	67.71 ± 0.31
Al_2O_3	8.41 ± 0.05	10.96 ± 0.11	7.15 ± 0.04	4.84 ± 0.08	8.44 ± 0.05	7.78 ± 0.08
Fe_2O_3	0.88 ± 0.00	1.64 ± 0.02	3.25 ± 0.01	0.64 ± 0.01	1.66 ± 0.00	2.01 ± 0.01
MnO	0.10 ± 0.00	4.74 ± 0.03	0.09 ± 0.00	1.35 ± 0.01	0.04 ± 0.00	0.05 ± 0.00
MgO	0.41 ± 0.01	0.65 ± 0.03	0.18 ± 0.01	1.27 ± 0.05	0.29 ± 0.01	0.38 ± 0.03
CaO	0.18 ± 0.01	0.68 ± 0.03	0.08 ± 0.01	1.47 ± 0.04	0.11 ± 0.01	3.92 ± 0.05
Na_2O	0.22 ± 0.01	0.42 ± 0.04	0.08 ± 0.01	0.27 ± 0.04	0.06 ± 0.01	0.08 ± 0.03
K_2O	3.79 ± 0.02	5.25 ± 0.05	3.79 ± 0.02	3.74 ± 0.05	4.01 ± 0.02	4.97 ± 0.04
TiO_2	0.35 ± 0.00	0.22 ± 0.00	0.14 ± 0.00	0.15 ± 0.00	0.35 ± 0.00	0.21 ± 0.00
BaO	0.12 ± 0.02	0.21 ± 0.08	0.06 ± 0.02	0.03 ± 0.07	0.05 ± 0.02	0.09 ± 0.06
P_2O_5	0.19 ± 0.02	0.27 ± 0.04	0.15 ± 0.02	0.17 ± 0.06	0.12 ± 0.02	0.18 ± 0.05
SO_3	0.15 ± 0.01	0.91 ± 0.04	0.40 ± 0.01	14.93 ± 0.17	0.18 ± 0.01	12.42 ± 0.12
Total	99.74	99.15	99.84	99.68	99.93	99.80

Uncertainties refer to the analytical technique. Measurement statistics did not allow for probing sample heterogeneity.

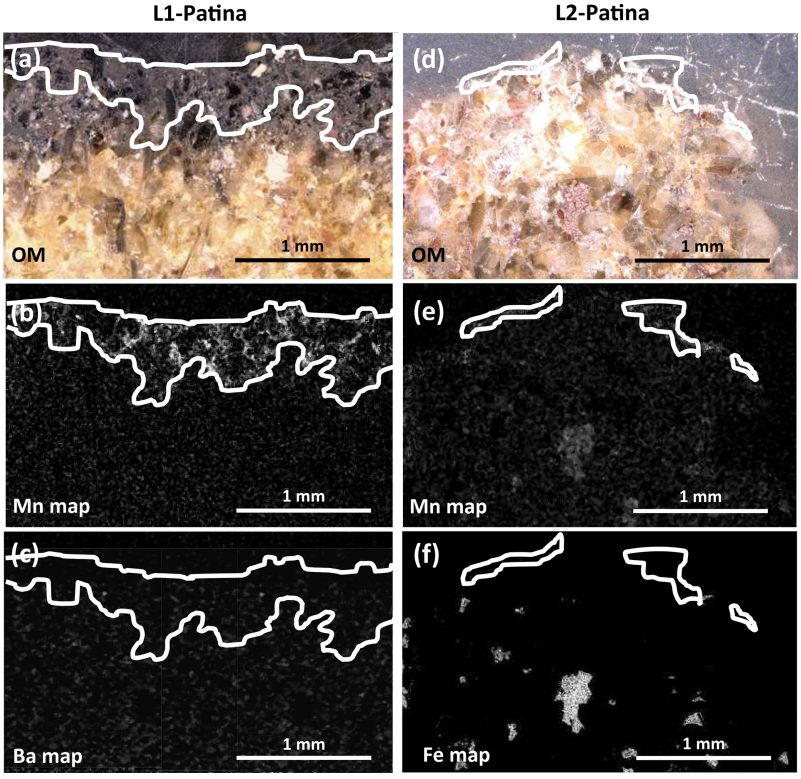

Figure 6. Optical images **(a, d)** and EDS maps **(b, c, e, f)** obtained on selected zones of L1 **(a, b, c)** and L2 **(d, e, f)** surfaces with patina. Areas in white outline extension of Mn-rich patinas. In the chemical maps, bright areas indicate high elemental concentrations (Mn: **b, e**; Ba: **c**; Fe: **f**).

3.2 Mn-bearing phase identification

Both μ-Raman spectroscopy and μ-XRD were used to gain further insights into the mineralogy of selected Mn-rich areas. Some of the collected Raman spectra or XRD patterns are typical of minerals present in Buntsandstein sandstones (quartz, feldspars, clay minerals, goethite, etc.) but will not be discussed hereafter as they are not relevant to identify Mn-bearing phases. No valuable results were obtained on L4 bulk, even in the most enriched zones, most likely because of the low Mn content. The 17 exploitable XRD patterns collected over two Mn-rich areas in L1 bulk are essentially similar and exhibit reflections at 3.46, 3.25–3.05, 2.40, 2.24–2.14, 1.87–1.80, 1.55, and 1.41 Å (Figs. 7a, S2). Similarly, the 24 Raman spectra collected over four Mn-rich areas (Fig. S3) display similar features differing only by minor variations in the relative intensities of the weakest bands (see Fig. 7b for a typical spectrum). Three major bands are observed at ~ 509, ~ 583, and $\sim 630\,cm^{-1}$, whereas three minor bands peak at ~ 183, ~ 290, and $\sim 405\,cm^{-1}$. Mn-rich areas in L1 bulk can thus be considered homogeneous and constituted of the same Mn mineral species whatever their position with respect to the block surface. Positions of XRD reflections are consistent with those of hollandite ($(Ba)_{1-2}Mn_8O_{16}$, xH_2O; Fig. 7a), in agreement with SEM analyses that show the systematic association of Mn and Ba (Fig. 5a–c). Although consistent with hollandite, Raman spectra are significantly broadened compared to natural hollandite (Fig. 7c), especially over the ~ 550–$750\,cm^{-1}$ range, most likely owing to low crystallinity (Colomban, 2013; Post, 1999; Baddour-Hadjean and Pereira-Ramos, 2010; Post et al., 2020). Additional broadening is possibly related to the admixture of Mn oxides, such as romanechite ($Ba_2Mn_5O_{10}$, xH_2O) or cryptomelane ($K_{1-2}Mn_8O_{16}$, xH_2O), with hollandite in the analyzed areas (Julien et al., 2004; Sepulveda et al., 2015; Post et al., 2020), consistent with XRD data (Fig. 7a).

The 11 Raman spectra collected in the L1 patina are similar with six Raman bands at ~ 294, ~ 400, ~ 503, ~ 583, ~ 649, and $\sim 733\,cm^{-1}$ (Figs. 7b, SI4) and correspond to birnessite ((Na,Ca,K)(Mg,Mn) Mn_6O_{14}, xH_2O; Julien et al., 2003, 2004). Although the birnessite spectral signature varies as a function of its layer structure (Julien et al., 2003), the L1 patina could be composed of birnessite having orthogonal (500, 578, $640\,cm^{-1}$) or hexagonal (296, 506, 575, 646, and $730\,cm^{-1}$) layer symmetry. The μ-XRD diffractograms on the L1 patina exhibit more variability than those obtained on the bulk (Fig. S5), mainly related to the additional presence of mineral contributions from quartz, mica, kaolinite, or gypsum (non-labeled peaks in Fig. 7a). The two *hk* bands at 2.40–2.45 and 1.41–1.42 Å, typical for disordered birnessite (δ-MnO_2), are, however, systematically present in XRD patterns obtained from the L1 patina (Fig. 7a).

The μ-XRD patterns collected on both L2 bulk and patina (data not shown) did not allow the identification of Mn-rich minerals, with goethite, magnetite–maghemite, quartz, and gypsum being the only minerals identified. Among the measured Raman spectra (9 for the bulk and 12 for the patina), only three for the bulk and two for the patina were suitable for Mn species identification owing to the low ratio between the Raman activity of the Mn species and the fluorescence signal. In addition, the low stability of Mn species did not allow laser power or data collection time to be increased, leading to data with a low signal-to-noise ratio. A quick alteration of pristine Mn phases during data collection is thus possible, and interpretation should thus be considered cautiously. The three Raman spectra collected in Mn-rich areas of L2 bulk display a broad intense band between 550 and $730\,cm^{-1}$ and weaker bands at 390–400 and 495–$505\,cm^{-1}$ (Fig. 8). One of the three spectra shows additional bands at 245 and $297\,cm^{-1}$. Mn and Fe being frequently associated in the bulk (Fig. 5e, f), these spectra possibly combine signatures of both Mn and Fe compounds. This hypothesis is supported by the intense Raman signal between 660 and $730\,cm^{-1}$ that corresponds to the most intense maghemite–magnetite bands at 665–670 and $730\,cm^{-1}$ and/or ferrihydrite ones at $710\,cm^{-1}$ (Hanesch, 2009).

The two spectra obtained for the L2 patina are poorly structured (Fig. 8) and contrast strikingly from those collected in the bulk, with a main band at 620–$625\,cm^{-1}$ possibly flanked by two shoulders ("L2-Patina-1" in Fig. 8). These patterns resemble those of lithiophorite ($Al_2LiMn_3O_6(OH)_6$) that exhibits a major Raman band at ~ 585–$640\,cm^{-1}$ (Julien et al., 2003). Consistent with the low Fe contents (Fig. 6f), the signal between 660 and $730\,cm^{-1}$ is absent from spectra collected on the L2 patina.

3.3 Mn-oxidation state

Complementary data on Mn-bearing phases have been obtained by measuring X-ray absorption spectra at the Mn K-edge (Figs. 9–11, Tables 2–4). L1 and L2 spectra present a much higher signal-to-noise ratio (Figs. 9 and 10) than L4 spectra (Fig. 11) due to the higher Mn content (Table 1).

The μ-XANES spectra collected at the Mn K-edge in L1 bulk are similar both within a given Mn-rich area and in different areas, independent of the distance from the surface, consistent with μ-XRD and Raman results. Typical pre-edges of XANES spectra (Fig. 9) are indicative of a 4+ manganese average oxidation state (Manceau et al., 1992; Chalmin, 2003; Farges, 2005; Ferrand, 2014; Ferrand et al., 2015), consistent with values determined using the Combo method that range from 3.73 to 4.00 (Table 2). Mn-rich areas in L1 bulk are mainly composed of Mn(IV) with some contributions from Mn(III), and almost no Mn(II) ($\geq 74\,\%$, $0\,\%$–$28\,\%$, and $\leq 12\,\%$, respectively; Table 2). These results are consistent with the presence of hollandite, a Mn oxide hosting mainly Mn(IV) and smaller amounts of Mn(III) and Mn(II), deduced from μ-XRD and μ-Raman spectroscopy. Manceau et al. (2012) obtained an average oxidation state of 3.81 for natural hollandite, with 82 % Mn(IV), 16 % Mn(III),

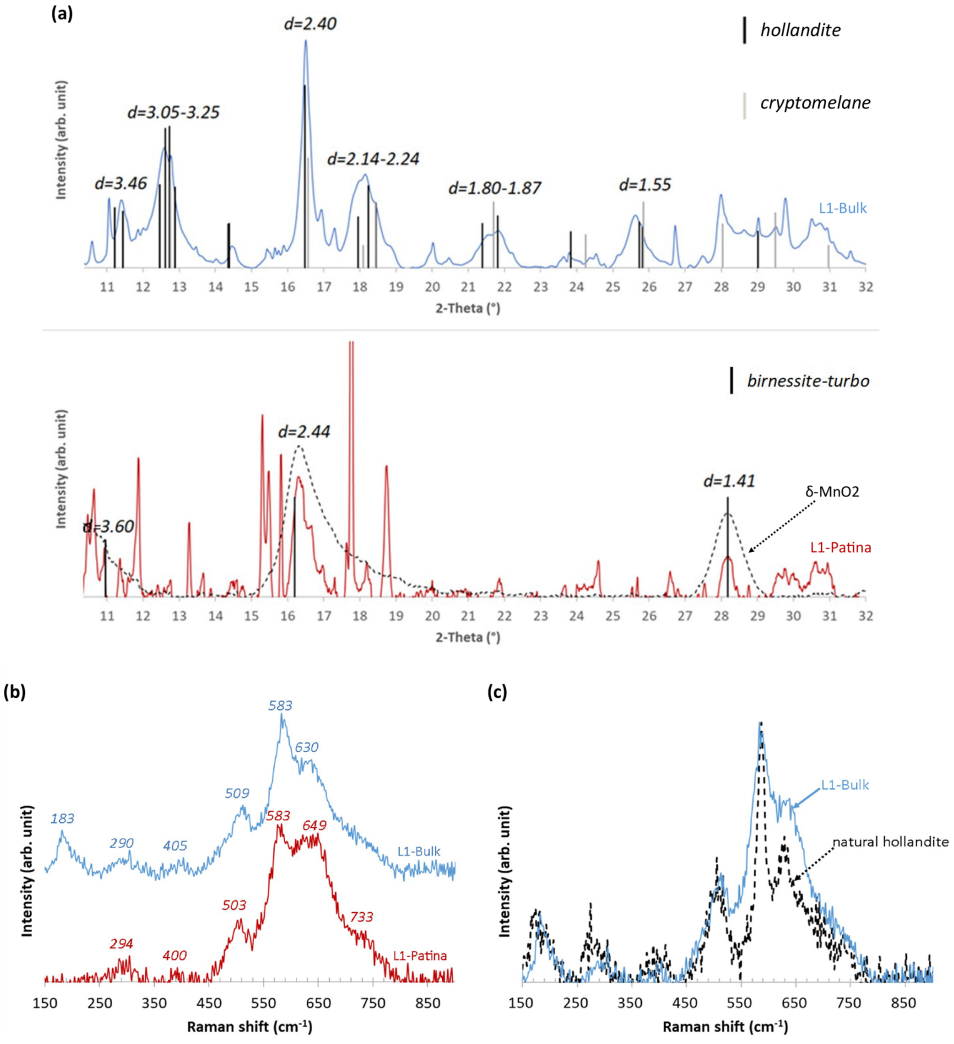

Figure 7. Representative **(a)** XRD patterns and **(b)** Raman spectra obtained for Mn-rich phases from L1 bulk and patina. δ-MnO_2 was synthesized as described by Grangeon et al. (2008). **(c)** Comparison of a representative Raman spectrum obtained from L1 bulk with that of natural hollandite.

Table 2. Relative proportions of Mn(II), Mn(III), and Mn(IV) determined using the Combo method in L1 regions of interest.

	Deep bulk		Subsurface		Patina
	Zone #4 (4 points)	Zone #3 (3 points)	Zone #2 (3 points)	Zone #1 (4 points)	(6 points)
Mn(II)	0 %–7 %	0 %–12 %	0 %–10 %	0 %–10 %	0 %–11 %
Mn(III)	0 %–26 %	0 %–24 %	0 %–10 %	0 %–28 %	0 %–21 %
Mn(IV)	76 %–100 %	75 %–100 %	81 %–100 %	74 %–100 %	76 %–100 %
Mn ox. state	3.73–4.00				3.76–4.00

"Zone #*n*" refers to black Mn-rich areas similar to those shown in Fig. 5, *n* increasing with the distance from the block surface. The ranges indicate data variability within a given zone, including measurement uncertainties.

and 2 % Mn(II). The µ-XANES spectra collected on the L1 patina also indicate a homogeneous composition (Fig. 9), with a major contribution from Mn(IV) ($\geq$ 76 %) and minor one from Mn(III) (0 %–21 %) and Mn(II) ($\leq$ 11 %; Table 2), resulting in an average Mn oxidation state ranging from 3.76 to 4.00. In contrast to µ-XRD and µ-Raman data, µ-XANES spectra collected over Mn-rich zones of both L1 bulk and L1 patina (Fig. 9, Table 2) are alike, consistent with the minor contrast of XANES spectra reported for hollandite and birnessite (Manceau et al., 2012; Ferrand, 2014).

Table 3. Relative proportions of Mn(II), Mn(III), and Mn(IV) determined using the Combo method in L2 regions of interest.

	Deep bulk		Subsurface		Patina		
	Zone #4 (3 points)	Zone #3 (3 points)	Zone #2 (5 points)	Zone #1 (3 points)	Light patina (3 points)	Intermediate patina (2 points)	Dark patina (5 points)
Mn(II)	0 %–47 %	0 %–51 %	29 %–88 %	23 %–100 %	54 %–93 %	52 %–64 %	19 %–34 %
Mn(III)	50 %–100 %	47 %–100 %	23 %–73 %	0 %–56 %	0 %–37 %	0 %–48 %	0 %–9 %
Mn(IV)	0 %	0 %–20 %	0 %	0 %–58 %	0 %–31 %	0 %–60 %	54 %–90 %
Mn ox. state	2.60–3.11		2.04–2.73		2.21–2.82		3.34–3.56

"Zone #*n*" refers to brown Mn-rich areas similar to those shown in Fig. 5, *n* increasing with the distance from the block surface. The ranges indicate data variability within a given zone, including measurement uncertainties.

Table 4. Relative proportions of Mn(II), Mn(III), and Mn(IV) determined using the Combo method in L4 regions of interest.

	Deep bulk				Subsurface	
	Black zones		Brown zones		Brown zones	
	Zone #4 (1 point)	Zone #3 (1 point)	Zone #4 (2 points)	Zone #3 (1 point)	Zone #2 (3 points)	Zone #1 (3 points)
Mn(II)	0 %	0 %–6 %	0 %	0 %	0 %	0 %
Mn(III)	19 %–27 %	0 %	82 %–100 %	76 %–100 %	71 %–100 %	81 %–100 %
Mn(IV)	75 %–79 %	94 %–100 %	0	0 %–18 %	0 %–31 %	0 %–6 %
Mn ox. state	3.73–4.00		2.94–3.15		2.94–3.21	

"Zone #*n*" refers to black or brown Mn-rich areas similar to those shown in Fig. 5, *n* increasing with the distance from the block surface. The ranges indicate data variability within a given zone, including measurement uncertainties.

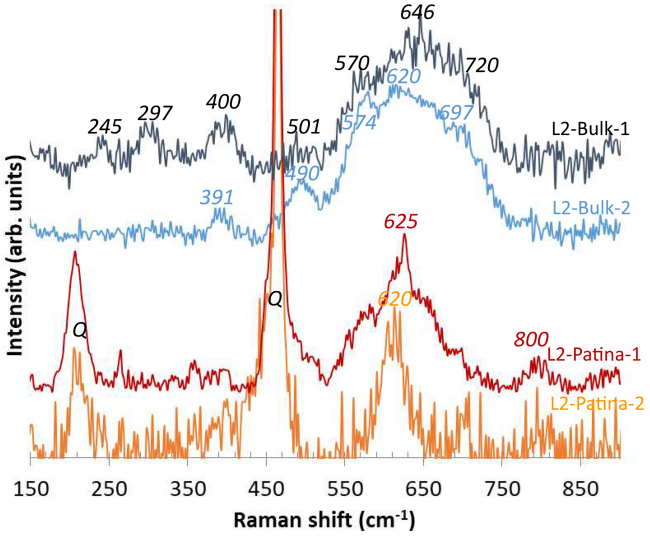

Figure 8. Representative Raman spectra obtained for Mn-rich phases from L2 bulk and patina. *Q* indicates quartz bands.

In contrast to homogeneous results obtained on L1, µ-XANES spectra collected on L2 vary significantly as a function of the distance from the block surface (Fig. 10). Mn-rich zones located in the block subsurface present a lower oxidation state (2.04–2.73) and a greater Mn(II) content (23 %–100 %) than zones deeper into the bulk (2.60–3.11 and 0 %–51 %, respectively; Table 3). Consistently, Mn is mainly present as Mn(III) in these deep bulk zones (47 %–100 %), whereas Mn(III) contents are lower in the subsurface (23 %–73 %). In both deep and subsurface bulk areas Mn(IV) is essentially absent (Table 3). The µ-XANES spectra obtained in the L2 patina are also variable, highlighting L2 patina heterogeneity; light and dark colored areas of the patina correspond to apparent extreme low and high values of Mn oxidation state, respectively (Figs. 2 and 10). In the "light patina", Mn(II) prevails over Mn(III) and Mn(IV) (≥ 54, ≤ 37 %, and ≤ 31 %, respectively; Table 3) leading to a Mn average oxidation state ranging from 2.21 to 2.82. Contrastingly, Mn(IV) dominates in "dark patina" (54 %–90 %), coexisting with Mn(II) (19 %–34 %) and minor Mn(III) (< 10 %; Table 3); Mn average oxidation state ranges from 3.34 to 3.56 in "dark patina". Spectra intermediate between these two end-members ("intermediate patina" – spectra not shown) were also collected in "dark patina" areas, indicative of the possible mixing of the different Mn-bearing phases coexisting in the L2 patina, although they are preferentially located in distinct areas, dark patina being more commonly observed in the vicinity of mortar patches.

Despite their low signal-to-noise ratio, µ-XANES spectra collected on the black Mn-rich areas of L4 indicate the prevalence of Mn(IV) (≥ 75 %), and the Mn average oxidation state ranges from 3.73 to 4.00 (Table 4, Fig. 11c). Compared to these black areas, brown Mn-rich zones are characterized by a higher Fe content (Fig. 5j–l), prevalence

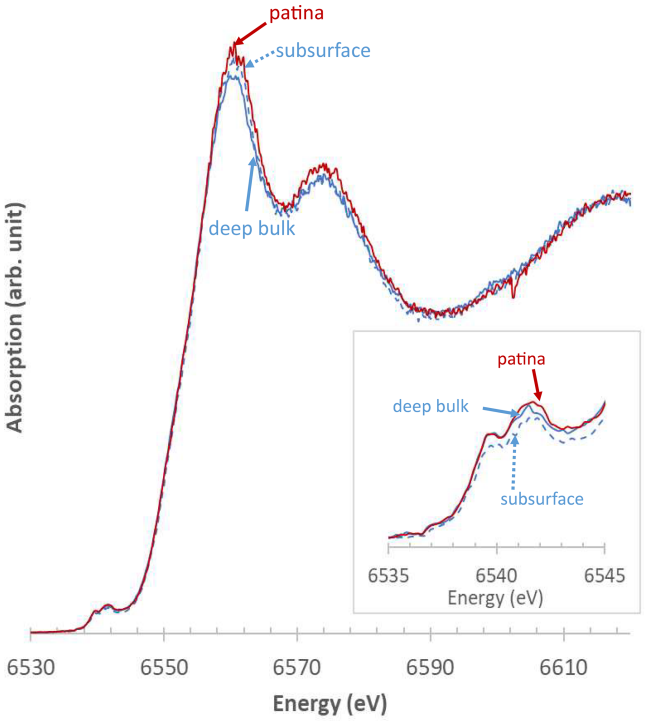

Figure 9. Representative XANES spectra obtained at the Mn K-edge from Mn-rich zones of L1. Solid blue line: bulk; dashed blue line: subsurface; solid red line: patina. Inset: zoom-in on the pre-edge region.

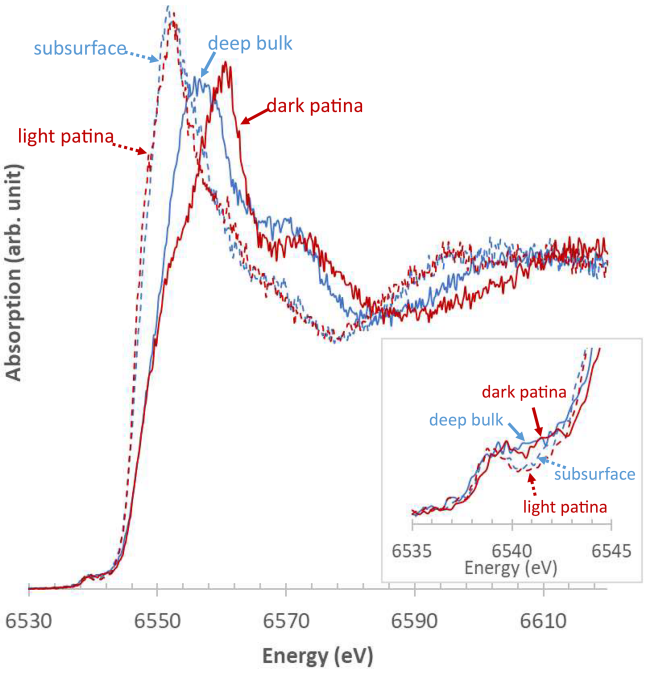

Figure 10. Representative XANES spectra obtained at the Mn K-edge from Mn-rich zones of L2. Solid blue line: deep bulk; dashed blue line: subsurface; dashed red line: lightly colored patina; solid red line: dark patina. Inset: zoom-in on the pre-edge region.

of Mn(III) ($\geq 71\,\%$), and lower Mn average oxidation state (2.94–3.21; Table 4, Fig. 11c). The occurrence of either type of Mn-bearing phase does not appear to be correlated with the distance from the block surface (Table 4).

4 Discussion

Over both unburnt and burnt areas of Lunéville château, patinas are characterized by high Mn contents compared to bulk compositions and to the composition of a patina-free sandstone surface (Table 1). The hypothesis of an external source of Mn was dismissed both because no external source could be identified and because such an external source would have resulted in a more homogeneous or azimuthally oriented distribution of areas exhibiting patinas. Furthermore, the possible aerial deposition of Mn originating from automotive traffic would most likely be associated with a significant enrichment in other "traffic-related" elements such as Ba, Zn, or Pb (Macholdt et al., 2017; Ortiz-Montalvo et al., 2018; Sharps et al., 2020), and that was not detected. In addition, the contribution of such an external "traffic-related" source of Mn is expected to be minor in the center of a small town ($\sim 18\,000$ inhabitants as of 2018) with cobbled streets. Mn thus most likely originates from Mn-bearing phases present in the pristine Buntsandstein sandstones.

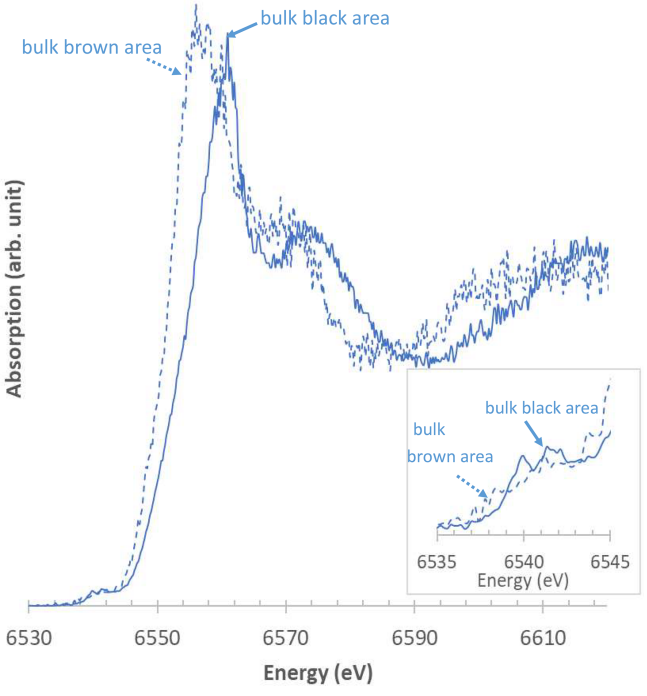

Figure 11. Representative XANES spectra obtained at the Mn K-edge from Mn-rich zones of L4. Dashed blue line: bulk brown zones; solid blue line: bulk black zones. Inset: zoom-in on the pre-edge region.

4.1 Natural formation of patina

Both L1 and L4 blocks were unaffected by the 2003 fire and have only been exposed to meteoric water. Penetration depth of rain water within building stones is difficult to assess because of the discontinuous stone–water contact and because only a fraction of rain water penetrates in the porous network on vertical surfaces. From previous estimates, only the superficial 2–5 cm of building stones are affected by rain water (Thomachot, 2002; Beck, 2006). Deep parts of L1 and L4 bulks thus likely provide a realistic description of Mn phases present in pristine sandstone blocks used to erect the château before any possible subsequent Mn leaching and patina formation. In both L1 and L4 deep bulks, Mn phases are clustered in brown and black areas. Mn is mainly present as Mn(III) in brown areas that are also enriched in Fe compared to the bulk. In black areas, Mn is mainly present as Mn(IV); no specific additional elemental enrichment was observed in L4 black areas, whereas those of L1 are enriched in Ba (Figs. 5, 9, and 11; Tables 2, 4). Low Mn contents in L4 (Table 1) did not allow for the mineralogical identification of Mn-bearing phases, whereas hollandite was identified as the main Mn-bearing mineral in L1 bulk (Fig. 7). Similar results were obtained in subsurface sections of L1 and L4 bulks, suggesting little alteration of Mn-bearing minerals when in contact with rain water.

The contrasting nature of the main Mn-bearing mineral identified in the L1 patina, birnessite, allows, however, the sole physical transportation of Mn-bearing phases from sandstone bulk to surface to be rejected as a possible explanation for natural formation of patina. Natural formation of patina observed on L1 block thus likely results from the precipitation of birnessite following the dissolution of initial Mn-bearing phases by rain water, a mechanism similar to that proposed for patina formation on Strasbourg cathedral (Nord and Ericsson, 1993). Morphological similarities of L1 patinas with those of Strasbourg cathedral (Thomachot, 2002) support this hypothesis. Contrastingly, Sharps et al. (2020) hypothesized from petrographic considerations that Ba and Mn forming the black layer on the Smithsonian Castle (Washington, DC) were sourced from atmospheric deposition. In both Lunéville château and Strasbourg cathedral cases, patinas are black and homogeneous in color over the block surface; in addition, patina minerals are intimately intergrown within subsurface sandstone grains over ~ 1 mm in Strasbourg cathedral and ~ 300–600 µm in Lunéville château (Fig. 6). Patinas from Strasbourg cathedral are strikingly different from the chemical point of view, however, being mainly Fe-rich without significant Mn contents. A similar dissolution and precipitation mechanism is also thought to be responsible for the formation of Mn soil nodules (Post, 1999; Manceau et al., 2003, 2005), in which phyllomanganates dominate Mn mineralogy, as in the L1 patina, possibly alternating with layers of Fe oxides. The actual mechanism responsible for patina formation remains ambiguous, however. Although not documented in the present study, the presence of Mn-oxidizing micro-organisms, bacteria but also fungi, is indeed required for the observed precipitation of Mn-bearing phases, abiotic Mn(II) oxidation being kinetically hindered (Tebo and He, 1999; Tebo et al., 2004). No experimental evidence for this likely biological pathway was sought or observed as part of the present study, however. Photo-chemical enhancement of this oxidative process is also possible, whereas alternation of wetting and drying cycles over time likely favors the thickening and homogeneity of the formed patina, together with a more complete oxidation of formed Mn-bearing phases. The absence of patina and of any significant Mn enrichment at the surface of L4 is most likely due to its ~ 60 % lower Mn content compared to L1 (Table 1, Fig. 5). Similar low Mn concentrations were consistently determined in the bulk of another patina-free sandstone block coming from a zone affected by the 2003 fire (L5 block in Gatuingt, 2017). L4 has indeed slightly higher porosity and capillarity than L1 that facilitate rain water access to Mn-rich zones of L4 bulk, compared to L1, the two blocks having similar permeability values (Gatuingt et al., 2016).

4.2 Patina formation as the result of the 2003 fire

The actual nature of Mn-bearing phases present in pristine L2 sandstone remains undetermined as the large volume of water used to extinguish the fire was sufficient to soak the château walls from surface to bulk, allowing for the alteration of initial Mn compounds even in the deepest parts of the bulk. Mineral aqueous alteration is expected to be lower in these deep zones compared to more superficial ones, however (Rousset-Tournier, 2001). This trend is consistent with the higher Mn oxidation states determined from XANES analyses in deep parts of L2 bulk that are dominated by Mn(III), compared to the L2 subsurface where Mn(II) consistently prevails (Table 3), although the morphology and chemical composition of Mn-rich zones are similar throughout L2 bulk (Fig. 5). Similarities between L2 deep bulk Mn-rich areas and "brown" Mn-rich zones in L4 bulk (morphology, association with Fe, Mn(III) prevalence) suggest that the initial Mn mineralogy was similar in both samples. In turn, the presence of Mn(II) in L2 bulk subsurface likely results from the reductive dissolution of Mn(III)-rich phases initially present (Bricker, 1965; Crerar et al., 1980; Martin, 2005) owing to the complete block imbibition by fire control water. As for the natural patina formation, a dissolution and precipitation mechanism is thus likely responsible for the formation of the L2 patina as the result of the 2003 fire. In addition to the observed Mn(II) gradient observed as a function of the distance from the block surface, this hypothesis is supported by contrasting Raman signatures obtained for Mn-bearing phases in L2 bulk and patina (Fig. 8), although these phases were not precisely identified. Moreover, high Mn(II) contents measured in the L2 patina (Table 3) are also con-

sistent with this reductive dissolution mechanism and with the induced sudden release of large amounts of Mn(II) to solution. Variability in Mn oxidation state in the L2 patina likely results from chemical conditions existing locally at the time of Mn(II) oxidation. In particular, high pH conditions prevailing close to mortar patches likely favor Mn oxidation (Bricker, 1965; Martin, 2005), resulting in the systematic prevalence of Mn(IV) (Table 3, dark areas). By contrast, Mn(II) to Mn(III) oxidation and/or Mn(III) stabilization are likely favored in L2 "light patina" zones, possibly as the result of lower pH conditions, consistent with the formation of metastable Mn_3O_4 and MnOOH phases as the result of Mn(II) oxidation at pH values ranging from 7 to 9 and room temperature (Hem, 1981; Hem and Lind, 1983; Murray et al., 1984).

4.3 Differences between natural and accidental patinas

The formation mechanism of both L1 and L2 patinas is thus likely the same with the initial dissolution of Mn-rich phases present in the pristine sandstone and the subsequent precipitation of different Mn-rich phases at the block surface following migration of soluble Mn(II) species. Despite their similar overall morphology and chemical composition, natural and accidental patinas exhibit differences, however. The natural L1 patina is darker, thicker, more homogeneous, and richer in Mn, and more especially in Mn(IV), than the accidental L2 patina; Mn-rich phases from the L1 patina also possess higher crystallinity that allowed their identification as birnessite from XRD patterns and Raman spectra (Fig. 7). Differences between the two patinas are possibly due to kinetic effects: in parts of the château not affected by the 2003 fire, dissolution of initial Mn-bearing phases and subsequent patina formation result from numerous imbibition and drying cycles or rainy episodes, allowing for complete oxidation and even recrystallization of Mn-rich phases precipitated at the sandstone exposed surface. On the other hand, accidental patina results mainly from a single and recent dissolution and precipitation event. In this case, oxidation of dissolved Mn(II) depends on local chemical conditions, thus leading to the observed heterogeneous L2 patina with Mn(IV,III) and Mn(III,II) phases in dark and light areas, respectively. Homogenization of the L2 patina will likely occur in the future as the result of its subsequent exposure to rain episodes, allowing for partial recrystallization, crystallinity improvement, and enhanced oxidation of existing Mn(III,II) phases.

5 Conclusions

Mn-rich patinas formed on Lunéville château were characterized using a multi-technique approach: OM and SEM-EDS revealed that Mn-bearing phases do not uniformly coat block surfaces but are rather located between subsurface sandstone grains, consistent with previous reports of patinas on natural sandstones or building stones. PIXE analyses and SEM-EDS observations highlighted the higher Mn contents of the patinas compared to the bulks of samples. Dark Mn-rich zones, a few hundred micrometers in size, were detected in sandstone bulks, however, with correlated elemental associations with Ba (L1 bulk) or Fe (L2 and L4 bulk brown areas). The low crystallinity of Mn oxides present in the Buntsandstein sandstones and their high sensitivity to beam interactions hamper their precise identification (Post, 1999; Bargar et al., 2005; Garvie et al., 2008; Baddour-Hadjean and Pereira-Ramos, 2010; Manceau et al., 2012; Ferrand, 2014). The combined use of μ-Raman spectroscopy, μ-XRD, and μ-XANES implemented in the present study allowed, however, insights into their mineralogy to be gained. When results were obtained from different techniques, they systematically provided consistent identification of Mn-minerals.

The contrasting mineralogy of Mn-rich phases present in the bulk and in the patina of a given block suggests that Mn required for patina formation likely derives from the reductive dissolution of Mn-rich minerals present in pristine sandstones as no external Mn source could be identified. Hollandite is the main Mn phase present in L1 bulk, whereas an initial Mn-rich phase could not be identified in L2 possibly because they were partially reduced as the result of the complete block imbibition by fire control water. Mn then migrates as reduced soluble species from the bulk to the exposed surface of building blocks where it is oxidized again. The oxidation mechanisms remain undetermined. Patinas of Lunéville château developed "naturally" over time (L1 block), result from the alternation of wetting-reducing and drying-oxidizing cycles, and appear to be composed of birnessite, a layered Mn oxide. On the other hand, patinas forming subsequently to the 2003 fire result from this single accidental event. As a consequence, they form a much thinner and discontinuous layer at the sandstone surface ($\sim$ 0–150 μm compared to $\sim$ 300–600 μm for "natural" patinas). In addition, the crystallinity of the Mn-rich minerals forming the accidental patinas, tentatively identified as lithiophorite, is much lower than that of birnessite in natural patinas. Mn oxidation degree also appears higher in natural patinas compared to accidental ones, especially in light areas. Further studies are required to assess if the present findings, and more especially the local sourcing of elements forming the patinas, can be generalized to other contexts.

Data availability. Original data from the present study can be accessed at https://doi.org/10.26022/IEDA/111980, file "1980-1_LunevilleXANES-XRD-Raman_Data.zip" (Gatuingt et al., 2021).

Supplement. Supplementary data to this article includes X-ray diffraction patterns and Raman spectra collected on L1 Mn-rich regions of interest from L1 bulk and patina. Sup-

plement data to this article can be found online at https://doi.org/10.26022/IEDA/111980, file "1980-2_LunevilleXANES-XRD-Raman_SupplementaryData.zip" (Gatuingt et al., 2021). The supplement related to this article is available online at: https://doi.org/10.5194/ejm-33-687-2021-supplement.

Author contributions. LG, StR, and JDM conceived the study. LG performed the experiments and compiled and interpreted the results. CF, QL, SoR, and NT supervised Raman, PIXE, XRD, and XAS data collection, respectively. BL interpreted XRD data from Mn-rich phases. LG, StR, JDM, CF, OR, and BL contributed to the writing of the article.

Competing interests. The contact author has declared that neither they nor their co-authors have any competing interests.

Disclaimer. Publisher's note: Copernicus Publications remains neutral with regard to jurisdictional claims in published maps and institutional affiliations.

Special issue statement. This article is part of the special issue "Mineralogy of the built environment". It is not associated with a conference.

Acknowledgements. The authors thank Mikaël Guiavarc'h and Sylvain Janiec (LRMH, Champs-sur-Marne, and ISTO, Orléans, France) for their assistance with sample preparations. Valérie Magnin (ISTerre, Grenoble, France) is thanked for helping with XANES data collection on the LUCIA beamline. XANES references used for Combo fitting were kindly provided by Sylvain Grangeon (BRGM, Orléans, France), and the δ-MnO_2 XRD reference was synthesized by Martine Lanson (ISTerre, Grenoble, France). Cristian Mocuta (DiffAbs beamline, synchrotron SOLEIL) integrated the XRD images. The authors thank the NewAGLAE (ANR-10-EQPX-22), DiffAbs, and LUCIA teams and SOLEIL facilities for beamtime allocation. The authors also thank France-Lanord-Bichaton (Nancy, France) for continuous support and more specifically Recep Yildirim and Claude Marin for their constant and friendly interaction. Constructive comments and remarks by editor Carlos Rodriguez-Navarro, guest editor Kerstin Elert, Eduardo Molina, and one anonymous reviewer helped improve the initial submission.

Financial support. This research has been supported by France-Lanord-Bichaton (Nancy, France).

Review statement. This paper was edited by Kerstin Elert and reviewed by Eduardo Molina and one anonymous referee.

References

Baddour-Hadjean, R. and Pereira-Ramos, J. P.: Raman microspectrometry applied to the study of electrode materials for Lithium batteries, Chem. Rev., 110, 1278–1319, https://doi.org/10.1021/cr800344k, 2010.

Bargar, J. R., Tebo, B. M., Bergmann, U., Webb, S. M., Glatzel, P, Chiu, V. Q., and Villalobos, M.: Biotic and abiotic products of Mn(II) oxidation by spores of the marine Bacillus sp. strain SG-1, Am. Mineral., 90, 143–154, https://doi.org/10.2138/am.2005.1557, 2005.

Beck, K.: Etude des propriétés hydriques et des mécanismes d'altération de pierres calcaires à forte porosité, PhD thesis, Université d'Orléans, France, 226 pp., 2006.

Beyer, D.: Evolution of reservoir properties in the Lower Triassic aquifer sandstones of the Thuringian Syncline in Central Germany, dissertation, Friedrich Schiller University Jena, Germany, 221 pp., 1983.

Bricker, O.: Some stability relations in the system Mn-O_2-H_2O at 25 °C and one atmosphere total pressure, Am. Mineral., 50, 1296–1354, 1965.

Chalmin, E.: Caractérisation des oxydes de manganèse et usage des pigments noirs au Paléolithique supérieur, PhD thesis, Université Paris-Est Marne-la-Vallée, France, 382 pp., 2003.

Colas, E.: Impact de l'humidité et des solutions salines sur le comportement dimensionnel de grès du Buntsandstein: contribution à la sélection de faciès de restauration, PhD thesis, Université de Reims Champagne-Ardenne, France, 321 pp., 2011.

Colomban, P.: Imagerie Raman de matériaux et dispositifs nano/microhétérogènes, Techniques de l'ingénieur Innovations en matériaux avancés, 2013.

Crerar, D. A., Cormick, R. K., and Barnes, H. L.: Geochemistry of Manganese: an overview, in Geology and Geochemistry of Manganese, edited by: Varentsov, I. M. and Grasselly, G., Schweizerbart Science Publishers, Stuttgart, Germany, 293–334, 1980.

Dorn, R. I.: Rock varnish, in Geochemical Sediments and Landscapes, edited by: Nash, D. J. and McLaren, S. J., Blackwell Publishing Ltd, 246–297, https://doi.org/10.1002/9780470712917.ch8, 2007.

Engel, C. G. and Sharp, R. P.: Chemical data on desert varnish, GSA Bulletin, 69, 487–518, https://doi.org/10.1130/0016-7606(1958)69[487:CDODV]2.0.CO;2, 1958.

Farges, F.: Ab initio and experimental pre-edge investigations of the Mn K-edge XANES in oxide-type materials, Phys. Rev. B, 71, 155109, https://doi.org/10.1103/PhysRevB.71.155109, 2005.

Ferrand, J.: Le phénomène de brunissement des vitraux médiévaux: critères d'identification et nature de la phase d'altération, PhD thesis, Université Paris-Est Marne-la-Vallée, France, 207 pp., 2014.

Ferrand, J. Rossano, S., Loisel, C., Trcera, N., van Hullebusch, E. D., Bousta, F., and Pallot-Frossard, I.: Browning Phenomenon of Medieval Stained Glass Windows, Anal. Chem., 87, 3662–3669, https://doi.org/10.1021/ac504193z, 2015.

Garvie, L. A. J., Burt, D. M. and Buseck, P. R.: Nanometer-scale complexity, growth, and diagenesis in desert varnish, Geology, 36, 215–218, https://doi.org/10.1130/G24409A.1, 2008.

Gatuingt, L.: Etude des mécanismes de formation des patines manganésifères des grès du château de Lunéville, PhD thesis, Université Paris-Est, France, 277 pp., 2017.

Gatuingt, L., Rossano, S., Mertz, J. D., Lanson, B., and Rozenbaum, O.: Intrinsic parameters conditionning the formation of Mn-rich patinas on Luneville sandstones, in Science and Art: A Future for Stone, proceedings of the 13th International Congress on the Deterioration and Conservation of Stone, Paisley, Scotland, 6–10 September 2016, 317–324, 2016.

Gatuingt, L., Rossano, S., Mertz, J., Rozenbaum, O., Lanson, B., Fourdrin, C., Reguer, S., and Trcera, N.: XANES, XRD and Raman-spectroscopy data on Mn-rich phases on Lunéville château sandstones (patinas and bulks), Version 1.0, Interdisciplinary Earth Data Alliance (IEDA) [data set], https://doi.org/10.26022/IEDA/111980, 2021.

Gaviño, M., Hermosin, B., Vergès-Belmin, V., Nowik, W., and Sáiz-Jiménez, C.: New insights on the chemical nature of stone yellowing produced after laser cleaning, in Cultural Heritage Conservation and Environmental Impact Assessment by Non-Destructive Testing and Micro-Analysis, edited by: Janssens, K. and Van Grieken, R., CRC Press, London, United Kingdom, 149–157, https://doi.org/10.1201/9781482283983, 2005.

Goldsmith, Y., Stein, M., and Enzel, Y.: From dust to varnish: Geochemical constraints on rock varnish formation in the Negev Desert, Israel, Geochim. Cosmochim. Ac., 126, 97–111, https://doi.org/10.1016/j.gca.2013.10.040, 2014.

Grangeon, S., Lanson, B., Lanson, M., and Manceau, A.: Crystal structure of Ni-sorbed synthetic vernadite: a powder X-ray diffraction study, Mineral. Mag., 72, 1279–1291, https://doi.org/10.1180/minmag.2008.072.6.1279, 2008.

Hanesch, M.: Raman spectroscopy of iron oxides and (oxy)hydroxides at low laser power and possible applications in environmental magnetic studies, Geophys. J. Int., 61, 941–948, https://doi.org/10.1111/j.1365-246X.2009.04122.x, 2009.

Hem, J. D.: Rates of manganese oxidation in aqueous systems, Geochim. Cosmochim. Ac., 45, 1369–1374, https://doi.org/10.1016/0016-7037(81)90229-5, 1981.

Hem, J. D. and Lind, C. J.: Nonequilibrium models for predicting forms of precipitated manganese oxides, Geochim. Cosmochim. Ac., 47, 2037–2046, https://doi.org/10.1016/0016-7037(83)90219-3, 1983.

Julien, C., Massot, M., Baddour-Hadjean, R., Franger, S., Bach, S. and Pereira-Ramos, J. P.: Raman spectra of birnessite manganese dioxides, Solid State Ionics, 159, 345–356, https://doi.org/10.1016/S0167-2738(03)00035-3, 2003.

Julien, C. M., Massot, M., and Poinsignon, C.: Lattice vibrations of manganese oxides: Part I. Periodic structures, Spectrochim. Acta A, 60, 689–700, https://doi.org/10.1016/S1386-1425(03)00279-8, 2004.

Kosaka, N.: Etude expérimentale de l'interaction entre des solutions naturelles et des roches poreuses: contrôle géochimique et pétrophysique, PhD thesis, Université Louis Pasteur de Strasbourg, France, 217 pp., 1995.

Krumbein, W. E. and Jens, K.: Biogenic rock varnishes of the negev desert (Israel) an ecological study of iron and manganese transformation by cyanobacteria and fungi, Oecologia, 50, 25–38, https://doi.org/10.1007/BF00378791, 1981.

Macholdt, D. S., Jochuma, K. P., Pöhlker, C., Stoll, B., Weis, U., Weber, B., Müller, M., Kappl, M., Buhre, S., Kilcoyne, A. L. D., Weigand, M., Scholz, D., Al-Amri, A. M., and Andreae, M. O.: Microanalytical methods for in-situ high-resolution analysis of rock varnish at the micrometer to nanometer scale, Chem. Geol., 411, 57–68, https://doi.org/10.1016/j.chemgeo.2015.06.023, 2015.

Macholdt, D. S., Herrmann, S., Jochum, K. P., Kilcoyne, A. L. D. , Laubscher, T., Pfisterer, J. H. K., Pöhlker, C., Schwager, B., Weber, B., Weigand, M., Domke, K. F., and Andreae, M. O.: Black manganese-rich crusts on a Gothic cathedral, Atmos. Environ., 171, 205–220, https://doi.org/10.1016/j.atmosenv.2017.10.022, 2017.

Manceau, A., Gorshkov, A. I., and Drits, V. A.: Structural chemistry of Mn, Fe, Co, and Ni in Mn hydrous oxides; Part I, information from XANES spectroscopy, Am. Mineral., 77, 1133–1143, 1992.

Manceau, A., Tamura, N., Celestre, R. S., Macdowell, A. A., Geoffroy, N., Sposito, G., and Padmore, H. A.: Molecular-scale speciation of Zn and Ni in soil ferromanganese nodules from loess soils of the Mississippi Basin, Environ. Sci. Technol., 37, 75–80, https://doi.org/10.1021/es025748r, 2003.

Manceau, A., Tommaseo, C., Rihs, S., Geoffroy, N., Chateigner, D., Schlegel, M., Tisserand, D., Marcus, M. A., Tamura, N., and Chen, Z. S.: Natural speciation of Mn, Ni, and Zn at the micrometer scale in a clayey paddy soil using X-ray fluorescence, absorption, and diffraction, Geochim. Cosmochim. Ac., 69, 4007–4034, https://doi.org/10.1016/j.gca.2005.03.018, 2005.

Manceau, A., Marcus, M. A., and Grangeon, S.: Determination of Mn valence states in mixed-valent manganates by XANES spectroscopy, Am. Mineral., 97, 816–827, https://doi.org/10.2138/am.2012.3903, 2012.

Marszalek, M., Alexandrowicz, Z., and Rzepa, G.: Composition of weathering crusts on sandstones from natural outcrops and architectonic elements in an urban environment, Environ. Sci. Pollut. R., 16, 14023–14036, https://doi.org/10.1007/s11356-014-3312-y, 2014.

Martin, S. T.: Precipitation and Dissolution of Iron and Manganese Oxides, in "Environmental Catalysis", edited by: Grassian, V. H., CRC Press, Boca Raton, Florida, United States, 61–81, https://doi.org/10.1201/9781420027679, 2005.

McKeown, D. A. and Post, J. E.: Characterization of manganese oxide mineralogy in rock varnish and dendrites using X-ray absorption spectroscopy, Am. Mineral., 86, 701–713, https://doi.org/10.2138/am-2001-5-611, 2001

Mertz, J.-D.: Etat des lieux, diagnostic des pathologies et perspectives, in: Restauration des façades des monuments urbains – contraintes, problèmes et satisfactions, edited by: Carré, D., Ministère de la Culture et de la Communication, OPPIC, France, 8–13, 2010.

Murray, J. W., Dillard, J. G., Giovanoli, R., Moers, H., and Stumm, W.: Oxidation of Mn(II): Initial mineralogy, oxidation state and ageing, Geochim. Cosmochim. Ac., 49, 463–470, https://doi.org/10.1016/0016-7037(85)90038-9, 1984.

Nord, A. G. and Ericsson, T.: Chemical analysis of thin black layers on building stone, Studies in Conservation, 38, 25–35, https://doi.org/10.2307/1506389, 1993.

Ortiz-Montalvo, D. L., Vicenzi, E. P., Ritchie, N. W., Grissom, C. A., Livingston, R. A., Weldon-Yochim, Z., Conny, J. M., and Wight, S. A.: Chemical compound classification by elemental signatures in Castle dust using SEM automated X-ray particle analysis, Microsc. Microanal., 24, 718–719, https://doi.org/10.1017/S1431927618004087, 2018.

Pichon, L., Moignard, B., Lemasson, Q., Pacheco, C., and Walter, P.: Development of a Multi-Detector and a Systematic Imaging System on the AGLAE External Beam, Nucl. Instrum. Meth. B, 318, 27–31, https://doi.org/10.1016/j.nimb.2013.06.065, 2014.

Post, J. E.: Manganese oxide minerals: Crystal structures and economic and environmental significance, P. Natl. Acad. Sci. USA, 96, 3447–3454, https://doi.org/10.1073/pnas.96.7.3447, 1999.

Post, J. E., McKeown, D. A. and Heaney, P. J.: Raman spectroscopy study of manganese oxides: Tunnel structures, Am. Mineral., 105, 1175–1190, https://doi.org/10.2138/am-2020-7390, 2020.

Potter, R. M. and Rossman, G. R.: The tetravalent manganese oxides: identification, hydration, and structural relationships by infrared spectroscopy, Am. Mineral., 64, 1199–1218, 1979.

Rousset-Tournier, B.: Transfert par capillarité et évaporation dans des roches - rôle des structures de porosité, PhD thesis, Université Louis Pasteur de Strasbourg, France, 203 pp., 2001.

Schaffer, R. J.: The weathering of natural building stones, London H. M. Stationery Office, 149 pp., 1932.

Sepulveda, M., Gutierrez, S., Vallette, M. C., Standen, V. G., Arriaza, B. T., and Carcamo-Vega, J. J.: Micro-Raman spectral identification of manganese oxides black pigments in an archaeological context in Northern Chile, Heritage Science, 3, 32, https://doi.org/10.1186/s40494-015-0061-2, 2015.

Sharps, M. C., Grissom, C. A., and Vicenzi, E. P.: Nanoscale structure and compositional analysis of manganese oxide coatings on the Smithsonian Castle, Washington, DC, Chem. Geol., 537, 119486, https://doi.org/10.1016/j.chemgeo.2020.119486, 2020.

Siegesmund, S., Weiss, T., and Vollbrecht, A.: Natural stone, weathering phenomena, conservation strategies and case studies: introduction, Geo. Soc. S. P., 205, 1–7, https://doi.org/10.1144/GSL.SP.2002.205.01.01, 2002.

Soyk, D.: Diagenesis and reservoir quality of the Lower and Middle Buntsandstein (Lower Triassic), dissertation, Heidelberg University, Germany, 201 pp., 2015.

Tebo, B. M. and He, L. M.: Microbially mediated oxidative precipitation reactions. Mineral-water interfacial reactions, ACS Symposium Series, 715, 393–414, https://doi.org/10.1021/bk-1998-0715.ch020 , 1999.

Tebo, B. M., Bargar, J. R., Clement, B. G., Dick, G J., Murray, K. J., Parker, D., Verity, R., and Webb, S. M.: Biogenic manganese oxides: Properties and mechanisms of formation, Annu. Rev. Earth Pl. Sci., 32, 287–328, https://doi.org/10.1146/annurev.earth.32.101802.120213, 2004.

Thiagarajan, N. and Lee, S. T. A.: Trace-element evidence for the origin of desert varnish by direct aqueous atmospheric deposition, Earth Planet. Sc. Lett., 224, 131–141, https://doi.org/10.1016/j.epsl.2004.04.038, 2004.

Thomachot, C.: Modifications de propriétés pétrophysiques de grès soumis au gel ou recouverts “d’encroûtements noirs vernissés”, PhD thesis, Université Louis Pasteur de Strasbourg, France, 324 pp., 2002.

Thomachot, C. and Jeannette, D.: Effects of iron black varnish on petrophysical properties of building sandstone, Environ. Geol., 47, 119–131, https://doi.org/10.1007/s00254-004-1139-4, 2004.

Vicenzi, E. P., Grissom, C. A., Livingston, R. A., and Weldon-Yochim, Z.: Rock varnish on architectural stone: microscopy and analysis of nanoscale manganese oxide deposits on the Smithonian Castle, Washington DC, Heritage Science, 4, 26 https://doi.org/10.1186/s40494-016-0093-2, 2016.